

Simultaneous resetting of the muscovite K-Ar and monazite U-Pb geochronometers: a story of fluids

Romain Tartese, Gilles Ruffet, Marc Poujol, Philippe Boulvais, Trevor R. Ireland

▶ **To cite this version:**

Romain Tartese, Gilles Ruffet, Marc Poujol, Philippe Boulvais, Trevor R. Ireland. Simultaneous resetting of the muscovite K-Ar and monazite U-Pb geochronometers: a story of fluids. Terra Nova, 2011, 23 (6), pp.390-398. 10.1111/j.1365-3121.2011.01024.x . insu-00643497

HAL Id: insu-00643497
https://insu.hal.science/insu-00643497

Submitted on 6 Dec 2011

HAL is a multi-disciplinary open access archive for the deposit and dissemination of scientific research documents, whether they are published or not. The documents may come from teaching and research institutions in France or abroad, or from public or private research centers.

L'archive ouverte pluridisciplinaire **HAL**, est destinée au dépôt et à la diffusion de documents scientifiques de niveau recherche, publiés ou non, émanant des établissements d'enseignement et de recherche français ou étrangers, des laboratoires publics ou privés.

Simultaneous resetting of the muscovite K-Ar and monazite U-Pb geochronometers: a story of fluids

Romain Tartèse[1,2*], Gilles Ruffet[1,2], Marc Poujol[1,2], Philippe Boulvais[1,2] and Trevor R. Ireland[3]

[1]Université de Rennes 1, Géosciences Rennes, 35042 Rennes Cedex, France

[2]CNRS (CNRS/INSU) UMR 6118, Géosciences Rennes, 35042 Rennes Cedex, France

[3]Research School of Earth Sciences, Australian National University, Canberra, ACT 0200, Australia

*Corresponding author: R. Tartèse (romain.tartese@univ-rennes1.fr)

Phone: 0033 2 23 23 30 81

Fax: 0033 2 23 23 60 97

Running title: Geochronometers resetting by fluids.

Abstract

Although water is ubiquitous in the continental crust, its effect on geochronometers through mineral reequilibration is rarely taken into account. Here we present $^{40}Ar/^{39}Ar$ analyses on muscovite and U-Pb isotopic data on zircon and monazite from a Variscan syn-tectonic granite from western France. Both the K-Ar in the muscovite and U-Pb in the monazite isotopic systems were hydrothermally reset, whereas the U-Pb radiogenic system in most of the zircons was unaffected and dates the granite emplacement age. Titanium chemical maps obtained on muscovites from various dated samples display a spectacular overprinting of their magmatic zoning resulting from increasing fluid-rock interaction. These results reiterate the need to combine geochronological data with petrological, mineralogical and geochemical studies to accurately interpret ages obtained in this type of geodynamical settings.

Keywords

$^{40}Ar/^{39}Ar$ and U-Pb dating; Armorican Massif; Geochronology; Granite; Hydrothermal recrystallization

1. Introduction

Thermochronology is based on the Arrhenius diffusion law, where temperature is the only extrinsic parameter controlling diffusion and thereby closure of isotopic chronometers (Jäger, 1967; Dodson, 1973). However, the presence of fluids can enhance mineral reequilibration processes (e.g. Putnis, 2009) which can disturb isotopic systems (e.g. Villa, 1998; 2010). Indeed, numerous studies have demonstrated that recrystallization and/or reequilibration processes can induce disturbance of mica $^{40}Ar/^{39}Ar$ ages in metamorphic terranes (e.g. Chopin and Maluski, 1980; Hames and Cheney, 1997; Cheilletz et al., 1999; Giorgis et al., 2000; Di Vicenzo et al., 2001; 2004; 2006; Beltrando et al., 2009; Allaz et al., 2011) and also in granites (Alexandrov et al., 2002).

In the continental crust, large shear zones are often associated with granitic magmatism (e.g. Weinberg et al., 2004). $^{40}Ar/^{39}Ar$ dating of muscovites from these syn-kinematic granites represents a powerful tool to date granite cooling and therefore coeval shearing. To evaluate the potential effect of fluid-induced disturbance at sub-solidus conditions in a deforming magmatic environment, we focused on the Questembert peraluminous leucogranite emplaced along the South Armorican Shear Zone (SASZ; Fig. 1a and b) at shallow depth (1-2 kbar, Tartèse and Boulvais, 2010), implying a rapid cooling in this cold environment. Widespread syn-cooling S-C structures (Fig. 1c) demonstrate its syn-kinematic character (Berthé et al., 1979, Gapais, 1989). This leucogranite allows to study the behaviour of distinct isotopic systems under a fluid controlled environment. Indeed, petrographic features, whole-rock and mineral chemistry and oxygen isotopes evidence two stages of hydrothermal alteration: a high-T stage of magmatic fluid exsolution and a low-T stage involving post-crystallization fluids partly derived from the surface (Tartèse and Boulvais, 2010). Fluid circulation throughout the granite has likely been facilitated by the pervasive and vertical S and C planes formed during its cooling (e.g. Dipple and Ferry, 1992;

Streit and Cox, 1998). The present study shows that both the K-Ar in muscovite and the U-Pb in monazite radiogenic systems were hydrothermally reset. Without a proper approach, ages measured in such environment could therefore be wrongly interpreted, which could lead to erroneous constraints regarding geodynamical reconstructions.

2. $^{40}Ar/^{39}Ar$ and U-Pb geochronology

2.1. Muscovite $^{40}Ar/^{39}Ar$ dating

Euhedral to subeuhedral muscovite grains, with variably deformed shapes resulting from syn-deformation crystallization, were handpicked from the 0.25-1.50 mm fractions. Mineralogical and microstructural features are given in Tartèse and Boulvais (2010). Individual grains were analyzed by step-heating with an $^{40}Ar/^{39}Ar$ laser probe, following the procedure described in Ruffet et al. (1991; 1995). Details on the method are given in the Supplementary Material. $^{40}Ar/^{39}Ar$ analytical data are listed in Table 1, and corresponding age spectra are displayed in Figure 2. All errors in the text are reported at 2σ. Muscovite analyses display $^{40}Ar/^{39}Ar$ plateau dates ranging from 319.2 ± 0.9 Ma down to 303.4 ± 0.9 Ma (Fig. 2a). Individually, each plateau date could be interpreted as an intrusion cooling age, although they conjointly demonstrate a 16 Ma age span, leading potentially to a non-negligible bias for the age of the synchronous shearing. At first glance, this time span rules out a single phase emplacement history for the intrusion.

The oldest *c*. 319 Ma date is recorded in the undeformed QRT01 sample. All the other samples are characterized by pervasive ductile structures related to shearing along the SASZ (Fig. 1c), without correlation between strain intensity and/or vicinity to the SASZ and the measured dates. A possible interpretation could be that the 319 Ma “old” underformed sample represents a first granitic pulse prior to deformation. Multiple granitic pulses would have continued from *c.* 315 down to *c.* 303 Ma, a time span during which Tartèse et al. (2011)

proposed that the SASZ was active. Muscovite dates would thus image the cooling of successive pulses of magmas below the closure temperature of the muscovite K-Ar system. This scenario would nevertheless require an unrealistic 16 Ma long protracted magmatic activity.

2.2. Monazite and zircon U-Th-Pb dating

To get independent age constraints, U-Th-Pb analyses were performed on zircons and monazites separated from sample QRT07, using the SHRIMP II and SHRIMP-RG respectively (Research School of Earth Sciences, ANU). Analytical procedures followed the methods described in Williams (1998) and in Williams et al. (1996), respectively. Details on the method are given in the Supplementary Material. Isotopic compositions and corresponding dates are given in Table 2. All errors in the text are reported at 2σ. Monazite U-Pb data yield an intercept date of 306.5 ± 3.2 Ma (Fig. 3a), the regression line being anchored to the $^{207}Pb/^{206}Pb$ value of 0.856, calculated at 307 Ma using the single stage model of Stacey and Kramers (1975) as few analyses show slight common lead contamination. Zircon U-Pb data are more scattered (Fig. 3b). Four data are largely discordant and likely show the combined effects of common lead contamination and lead-loss. Seven concordant to sub-concordant analyses cluster around 310-320 Ma and yield a consistent $^{206}Pb/^{238}U$ weighted mean date of 316.1 ± 2.9 Ma. One analysis is significantly older and plots at *c.* 335 Ma.

BSE images of monazite grains display complex zoning patterns and/or dissolution features (Fig. 4b to 4e) reflecting chemical disequilibrium, while monazite in Fig. 4a seems to be homogeneous and shows a crack filled with K-Feldspar. The SE image displayed in Fig. 4f shows a monazite grain with K-Feldspar and zircon intergrowth. CL images of most of the zircon grains display cores with a typical magmatic oscillatory zoning (Fig. 4g to 4i) surrounded by darker homogeneous rims (Fig. 4h and 4i). The zoned domains yielded sub-

concordant dates around 317-318 Ma (Figs. 3b and 4g-h) whereas the analysis of a dark rim is largely discordant (Figs. 3b and 4h). Fig. 5 shows that the most discordant data are the most contaminated by common Pb. Common lead contamination likely occurred preferentially in metamict domains or in hydrothermal rims, potentially linked to a common Pb-rich fluid input in the system (e.g. Watson et al., 1997).

The first important result is that monazite and muscovite ages in sample QRT07 are consistent at *c*. 307 Ma while zircon grains are older at *c*. 316 Ma. Also, zircon displays typical magmatic zoning while monazite grains show patchy zoning and evidences of dissolution-recrystallization features. The grain textures and large difference between zircon and monazite U-Pb ages rule out the possibility that both date magmatic events. The second important result is that the zircon U-Pb age of 316.1 ± 2.9 Ma obtained on sample QRT07 is identical within error with the $^{40}Ar/^{39}Ar$ age of 319.2 ± 0.9 Ma obtained on sample QRT01.

3. Whole-rock and muscovite chemistry

$^{40}Ar/^{39}Ar$ dates have been compared to whole-rock geochemical data (from Tartèse and Boulvais, 2010). Dates show a good negative correlation with the whole-rock Sn content (Fig. 2b), an incompatible element concentrated in late magmatic fluids (Förster et al., 1999). A positive correlation is also noticeable with the Nb/Ta ratio (Fig. 2b), whose fractionation from a typical crustal ratio of around 11 has been interpreted as a strong indicator of fluid-rock interaction (Dostal and Chatterjee, 2000). The most altered samples, with high Sn contents and low Nb/Ta ratios, are also those yielding the youngest $^{40}Ar/^{39}Ar$ muscovite dates. Dates are thus getting younger when evidence of hydrothermal activity recorded by host rocks increases.

The chemistry of muscovite grains from the dated samples was also examined (for analytical details and chemical data, see Supplementary Material). These grains have a typical

magmatic shape and a size similar to the dated grains. Muscovite in the studied samples has a composition close to the stoichiometric muscovite (Si = 3.07 ± 0.02 and Al = 2.73 ± 0.04 apfu in average). In the Ti-Na-Mg diagram (Fig. 6a), the measured compositions encompass the field of primary (i.e. magmatic) and secondary (i.e. hydrothermal) muscovite (Miller et al., 1981). In detail, muscovite from the 319 Ma QRT01 sample plots within the primary field, muscovite from the 303 Ma QRT02 sample plots within the secondary field and muscovite from other samples ($^{40}Ar/^{39}Ar$ dates between 315 and 307 Ma) lies between these two end-members. When reported against the Mg/(Mg+Ti+Na) molar parameter (Fig. 6b), it becomes evident that muscovites are getting younger as their chemistry tends toward the hydrothermal field.

Chemical maps of the TiO_2 content (Fig. 7) were acquired in order to precisely image chemical changes induced by hydrothermal activity. In QRT01, the transition between a Ti-rich core and a Ti-poor rim is very sharp and typical of magmatic growth. It cannot be interpreted as a post-crystallization solid-state diffusion, which would have induced smooth changes. From QRT08 to QRT06 and then QRT02, these Ti-zonings are less marked and associated with an absolute decrease in TiO_2. We thus infer that all the studied grains have a magmatic origin and that most of them underwent hydrothermal alteration and recrystallization, such that they acquired secondary hydrothermal compositions. This hydrothermal alteration led to a progressive overprinting of their magmatic zoning and induced crystallo-chemical transformations throughout the entire grain (Fig. 7). In these conditions, it is very unlikely that the muscovite K-Ar isotopic system remained undisturbed.

4. Discussion

The six samples collected in the Questembert granite display different $^{40}Ar/^{39}Ar$ plateau ages, in the range 319-303 Ma, all potentially meaningfull when considered

individually. The question that arises is therefore how such a large time span can exist within a single rapidly cooled intrusion. Several scenarios can be drawn: (1) each individual $^{40}Ar/^{39}Ar$ age corresponds to a different magmatic pulse; (2) the intrusion was emplaced *c.* 303 Ma ago (youngest $^{40}Ar/^{39}Ar$ age) and all the older dates are meaningless and (3) the intrusion took place *c.* 319 Ma (oldest $^{40}Ar/^{39}Ar$ age) and all the younger ages are linked to hydrothermal alteration.

Several arguments allow us to favour the third scenario. The oldest $^{40}Ar/^{39}Ar$ and U-Pb dates at *c.* 319 Ma were obtained on muscovite and zircon grains that show typical magmatic textures. On the contrary, all the younger muscovite $^{40}Ar/^{39}Ar$ and monazite U-Pb dates were found on grains showing variable degrees of alteration and fluid-assisted recrystallization. This therefore rules out the first scenario of distinct magmatic pulses. In the second scenario, the older $^{40}Ar/^{39}Ar$ muscovite dates would reflect the contribution of extraneous argon (e.g. Damon et al., 1967). However, as the $^{40}Ar/^{39}Ar$ dates regularly decrease with the increase of the hydrothermal character recorded by both the whole-rock and the muscovite chemistry, the age span is much likely related to resetting of old ages than to excess Ar. This is consistent with the high level of emplacement of the granite along a major shear zone, i.e. in a fluid-dominated system which constitutes an inifinite reservoir where Ar can escape (e.g. Kelley, 2002). Also, the oldest muscovite $^{40}Ar/^{39}Ar$ date of *c.* 319 Ma is within error with the zircon U-Pb date of 316.1 ± 2.9 Ma, which is unlikely fortuitous. We rather interpret the 316-319 age as the emplacement age of the granite and the younger muscovite $^{40}Ar/^{39}Ar$ and monazite U-Pb dates as the results of hydrothermal sub-solidus alteration.

Two extreme hydrothermal scenarios may explain the observed data: (1) fluids flowed throughout the granite around 303 Ma and differentially re-equilibrated the various samples, depending on the fluid/rock ratio; (2) fluids flowed more or less continuously throughout the granite and were recorded locally at different times. Muscovite data favour the second

scenario. Indeed there is a progressive hydrothermal overprinting of the magmatic signal in muscovite grains caused by fluid-induced recrystallization. It is very unlikely that radiogenic argon, an unbounded and highly diffusive element, remained in the crystalline network of muscovite that undergoes crystallo-chemical transformations throughout the entire grain (Fig. 7). Moreover, hydrothermal scenario 1 would likely implied pronounced saddle-shaped $^{40}Ar/^{39}Ar$ age spectra expressing mixing between a *c*. 320 Ma magmatic and a *c*. 303 hydrothermal end-members (e.g. Cheilletz et al., 1999), which are not observed in Fig. 2a. Here, muscovite yielded only very subtle saddle-shaped age spectra testifying for distinct protracted (*c*. 1-2 Ma) recrystallization events. Monazite U-Pb dates also favour hydrothermal scenario 2. Analyses made on grains from sample QRT07 yield a consistent age of *c*. 307 Ma, identical within error with the $^{40}Ar/^{39}Ar$ date. K-Ar in muscovite and U-Pb in monazite therefore date hydrothermal resetting of both radiogenic systems. Still in sample QRT07, a couple of discordant zircon analyses have likely been affected by this event, but most of them have not as they preserved the granite emplacement age. Therefore, monazite has been totally reset by hydrothermal alteration whereas zircon did not. This is in good agreement with the fact that monazite is often more sensitive to fluid-rock interactions than zircon (Ayers et al., 2006; Bosse et al., 2009; Poujol et al., 2010). Finally, data show that a long lasting sequential and heterogeneous hydrothermal activity affected the granite after its emplacement. It may have been initiated by the release of high temperature magmatic fluids during granite solidification and continued for a long time with fluids derived from both the crust and the surface. This is in good agreement with the “two-stage alteration” that affected the Questembert granite (Tartèse and Boulvais, 2010), and with the intense hydrothermal activity that affected this part of the Variscan orogeny at the end of the Carboniferous (e.g. Gloaguen et al., 2007; Lemarchand et al., 2011).

5. Conclusion

The $^{40}Ar/^{39}Ar$ muscovite dates from six samples collected in a single syn-kinematic granite provide distinct and meaningful ages, covering a time span of 16 Ma. Considering the shallow depth of intrusion of the Questember granite (ca. 5 km), this time span cannot be interpreted as a slow cooling of the intrusion. Moreover, combined geochemical and complementary U-Pb isotope data demonstrate that this time span neither corresponds to a long magmatic activity nor to discrete deformation-related events. It is rather the consequence of a fluid-assisted resetting of the muscovite K-Ar and monazite U-Pb chronometers. As fluids are ubiquitous in the Earth, especially in highly deformed zones, this study shows that it is highly hazardous to interpret ages without detailed geochemical and crystallo-chemical investigations of the studied rocks and minerals.

Acknowledgments

R.T. acknowledges Rennes Métropole for the travel grant he received to go to the Australian National University, Canberra. We are grateful to M. Bohn and P. Holden for their assistance in the electron microprobe and SHRIMP analyses. This work was funded by grants from the CNRS-INSU (“3F” and “Action incitative” programs). Finally, J. Allaz, Y. Roland and G. Di Vicenzo and the associate editor I.M. Villa are sincerely thanked for their insightful comments.

References

Alexandrov, P., Ruffet, G. and Cheilletz, A., 2002. Muscovite recrystallization and saddle-shaped $^{40}Ar/^{39}Ar$ age spectra: Example from the Blond granite (Massif Central, France). *Geochim. Cosmochim. Ac.*, **66**, 1793-1807.

Allaz, J., Engi, M., Berger, A. and Villa, I.M., 2011. The effects of retrograde reactions and of diffusion on ^{40}Ar-^{39}Ar ages of micas. *J. Petrol.*, **52**, 691-716.

Ayers, J.C., Loflin, M., Miller, C.F., Barton, M.D. and Coath, C.D, 2006. In situ oxygen isotope analysis of monazite as a monitor of fluid infiltration during contact metamorphism: Birch Creek Pluton aureole, White Mountains, eastern California. *Geology*, **34**, 653-656.

Beltrando, M., Lister, G.S., Forster, M., Dunlap, W.J., Fraser, G. and Hermann, J., 2009. Dating microstructures by the $^{40}Ar/^{39}Ar$ step-heating technique: Deformation-pressure-temperature-time history of the Penninic Units of the Western Alps. *Lithos*, **113**, 801-819.

Berthé, D., Choukroune, P. and Jégouzo, P., 1979. Orthogneiss, mylonite and non coaxial deformation of granites - example of the South-Armorican-Shear-Zone. *J. Struct. Geol.*, **1**, 31-42.

Bosse, V., Boulvais, P., Gautier, P., Tiepolo, M., Ruffet, G., Devidal, J.-L., Cherneva, Z., Gerdjikov, I. and Paquette, J.-L., 2009. Fluid-induced disturbance of the monazite Th-Pb chronometer: In situ dating and element mapping in pegmatites from the Rhodope (Greece, Bulgaria). *Chem. Geol.*, **261**, 286-302.

Cheilletz, A., Ruffet, G., Marignac, C., Kolli, O., Gasquet, D., Féraud, G. and Bouillin, J.-P., 1999. $^{40}Ar/^{39}Ar$ dating of shear zones in the Variscan basement of Greater Kabylia (Algeria). Evidence of an Eo-Alpine event at 128 Ma (Hauterivian–Barremian boundary): geodynamic consequences. *Tectonophysics*, **306**, 97-116.

Chopin, C. and Maluski, H., 1980. ^{40}Ar-^{39}Ar dating of high pressure metamorphic micas from the Gran Paradiso area (Western Alps): evidence against the blocking temperature concept. *Contrib. Mineral. Petrol.*, **74**, 109-122.

Damon, P.E., Laughlin, A.W. and Percious, J.K., 1967. Problem of excess argon-40 in volcanic rocks. In: Radioactive dating and methods of low-level counting. International Atomic Energy Agency, Vienna, 463-481.

Dipple, G.M. and Ferry, J.M., 1992. Metasomatism and fluid flow in ductile fault zones. *Contrib. Mineral. Petrol.*, **112**, 149-164.

Di Vincenzo, G., Ghiribelli, B., Giorgetti, G. and Palmeri, R., 2001. Evidence of a close link between petrology and isotope records: constraints from SEM, EMP, TEM and in situ ^{40}Ar-^{39}Ar laser analyses on multiple generations of white micas (Lanterman Range, Antarctica). *Earth Planet. Sci. Lett.*, **192**, 389-405.

Di Vincenzo, G., Carosi, R. and Palmeri, R., 2004. The relationship between tectono-metamorphic evolution and argon isotope records in white mica: constraints from *in situ* ^{40}Ar-^{39}Ar laser analysis of theVariscan basement of Sardinia. *J. Petrol.*, **45**,1013-1043.

Di Vicenzo, G., Tonarini, S., Lombardo, B., Castelli, D. and Ottolini, L., 2006. Comparison of ^{40}Ar-^{39}Ar and Rb–Sr data on phengites from the UHP Brossasco-Isasca Unit (Dora Maira Massif, Italy): Implications for dating white mica. *J. Petrol.*, **47**,1439-1465.

Dodson, M.H., 1973. Closure temperature in cooling geochronological and petrological systems. *Contrib. Mineral. Petrol.*, **40**, 259-274.

Dostal, J. and Chatterjee, A.K., 2000. Contrasting behaviour of Nb/Ta and Zr/Hf ratios in a peraluminous granitic pluton (Nova Scotia, Canada). *Chem. Geol.*, **163**, 207-218.

Förster, H.J., Tischendorf, G., Trumbull, R.B. and Gottesmann, B., 1999. Late-collisonal granites in the Variscan Erzgebirge, Germany. *J. Petrol.*, **40**, 1613-1645.

Gapais, D., 1989. Shear structures within deformed granites - Mechanical and thermal indicators. *Geology*, **17**, 1144-1147.

Giorgis, D., Cosca, M. and Li, S., 2000. Distribution and significance of extraneous argon in UHP eclogite (Sulu terrain, China): insight from in situ $^{40}Ar/^{39}Ar$ UV-laser ablation analysis. *Earth Planet. Sci. Lett.*, **181**, 605-615.

Gloaguen, E., Branquet, Y., Boulvais, P., Moëlo, Y., Chauvel, J.-J., Chiappero, P.-J. and Marcoux, E., 2007. Palaeozoic oolitic ironstone of the French Armorican Massif: a chemical and structural trap for orogenic base metal-As-Sb-Au mineralisation during Hercynian strike-slip deformation. *Miner. Deposita*, **42**, 399-422.

Hames, W.E. and Cheney, J.T., 1997. On the loss of $^{40}Ar^{*}$ from muscovite during polymetamorphism. *Geochim. Cosmochim. Ac.*, **61**, 3863-3872.

Jäger, E., 1967. Die bedeutung der Biotit-Alterswerte. In: Rb-Sr Altersbestimmungen an Glimmern der Zentralalpen (E. Jäger, E. Niggli and E. Wenk, eds). Beiträge zur Geologischen Karte der Schweiz, **134**, 28-31.

Kelley, S., 2002. Excess argon in K-Ar and Ar-Ar geochronology. *Chem. Geol.*, **188**, 1-22.

Lemarchand, J., Boulvais, P., Gaboriau, M., Boiron, M.-C., Tartèse, R., Cokkinos, M., Bonnet, S. and Jégouzo, P., 2011. Giant quartz vein formation and high elevation meteoric fluid infiltration into the South Armorican Shear Zone: geological, fluid inclusion and stable isotope evidence. *J. Geol. Soc. Lond.*, in press. doi: 10.1144/0016-76492010-186.

Miller, C.F., Stoddard, E.F., Bradfish, L.J. and Dollase, W.A., 1981. Composition of plutonic muscovite: genetic implications. *Can. Mineral.*, **19**, 25-34.

Poujol, M., Boulvais, P. and Kosler, J., 2010. Regional-scale Cretaceous albitization in the Pyrenees: evidence from in situ U-Th-Pb dating of monazite, titanite and zircon. *J. Geol. Soc.*, **167**, 751-767.

Putnis, A., 2009. Mineral replacement reactions. *Rev. Mineral. Geochem.*, **70**, 87-124.

Renne P.R., Mundil R., Balco G., Min K., Ludwig K.R., 2010. Joint determination of ^{40}K decay constants and $^{40}Ar^*/^{40}K$ for the Fish Canyon sanidine standard, and improved accuracy for $^{40}Ar/^{39}Ar$ geochronology. *Geochim. Cosmochim. Ac.*, **74**, 5349-5367.

Ruffet, G., Féraud, G. and Amouric, M., 1991. Comparison of $^{40}Ar/^{39}Ar$ conventional and laser dating of biotites from the North Tregor batholiths. *Geochim. Cosmochim. Ac.*, **55**, 1675-1688.

Ruffet, G., Féraud, G., Ballèvre, M. and Kienast, J.R., 1995. Plateau ages and excess argon in phengites - An ^{40}Ar-^{39}Ar laser probe study of alpine micas (Sesia zone, Western Alps, northern Italy). *Chem. Geol.*, **121**, 327-343.

Stacey, H.S. and Kramers, J.D., 1975. Approximation of terrestrial lead isotope evolution by a 2-stage model. *Earth Planet. Sci. Lett.*, **26**, 207-221.

Steiger, R.H. and Jäger, E., 1977. Subcommission on geochronology: convention on the use of decay constants in geo- and cosmochronology. *Earth Planet. Sci. Lett.*, **36**, 359-362.

Streit, J.E. and Cox, S.F., 1998. Fluid infiltration and volume change during mid-crustal mylonitization of Proterozoic granite, King Island, Tasmania. *J. Metamorph. Geol.*, **16**, 197-212.

Tartèse, R. and Boulvais, P., 2010. Differentiation of peraluminous leucogranites "en route" to the surface. *Lithos*, **114**, 353-368.

Tartèse, R., Boulvais, P., Poujol, M., Chevalier, T., Paquette, J.-L., Ireland, T.R. and Deloule, E., 2011. Mylonites of the South Armorican Shear Zone: Insights for crustal-scale fluid flow and water-rock interaction processes. *J. Geodyn.*, in press. doi: 10.1016/j.jog.2011.05.003.

Villa, I.M., 1998. Isotopic closure. *Terra Nova*, **10**, 42-47.

Villa, I.M., 2010. Disequilibrium textures versus equilibrium modelling: geochronology at the crossroads. In: Advances in Interpretation of Geological Processes: Refinement of Multi-scale Data and Integration in Numerical Modelling (M.I. Spalla, A.M. Marotta and G. Grosso, eds). *Geol. Soc. Lond. Spec. Pub.*, **332**, 1-15.

Watson, E.B., Cherniak, D.J., Hanchar, J.M., Harrison, T.M. and Wark, D.A., 1997. The incorporation of Pb into zircon. *Chem. Geol.*, **141**, 19-31.

Weinberg, R.F., Sial, A. and Mariano, G., 2004. Close spatial relationship between plutons and shear zones. *Geology*, **32**, 377-380.

Williams, I.S., 1998. U-Th-Pb Geochronology by Ion Microprobe. In: Applications of Microanalytical Techniques to Understanding Mineralizing Processes (M.A. McKibben, W.C. Shanks III and W.I. Ridley, eds). Reviews in Economic Geology, Society of Economic Geologists, **7**, 1-35.

Williams, I.S., Buick, I.S. and Cartwright, I., 1996. An extended episode of early Mesoproterozoic metamorphic fluid flow in the Reynolds Range, central Australia. *J. Metam. Geol.*, **14**, 29-47.

Whitney, D.L. and Evans, B.W., 2010. Abbreviations for names of rock-forming minerals. *Am. Mineral.*, **95**, 185-187.

Figure captions

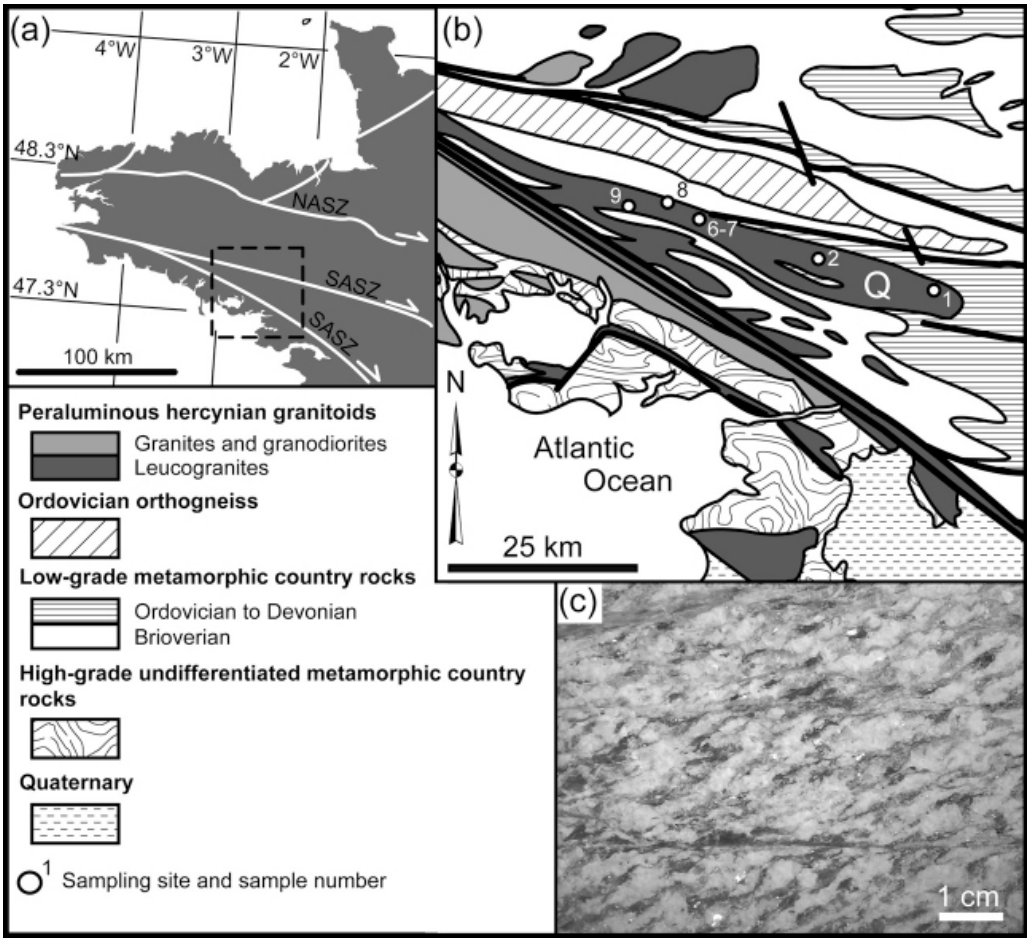


Figure 1: a) Localization of the studied area in the Armorican massif. NASZ: North Armorican Shear Zone; SASZ: South Armorican Shear Zone; b) Simplified geological map of the Questembert granite (Q) region; c) Photograph of sample QRT07 showing typical S-C structures, indicative of a syn-crystallization dextral shearing.

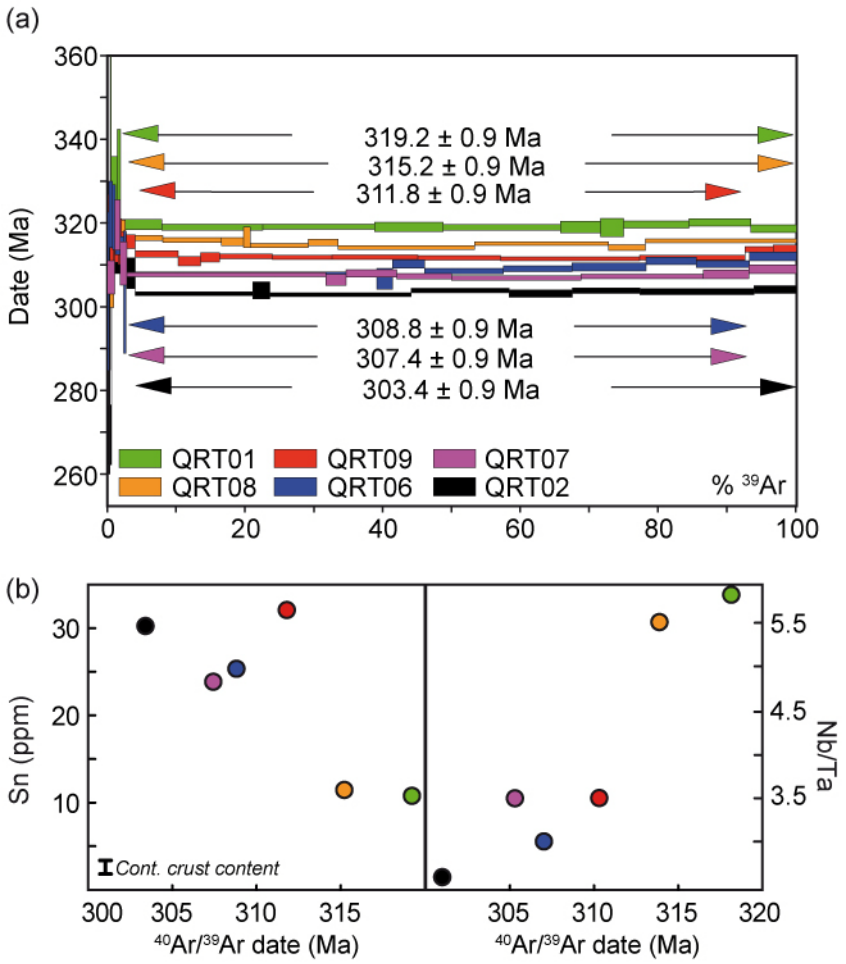


Figure 2: a) $^{40}Ar/^{39}Ar$ age spectra of analyzed muscovites. The age error bars for each temperature steps are at the 1σ level. Plateau ages are given with a 2σ uncertainty, including error on the decay constant (λ_{tot} = 5.5492 x 10^{-10} a^{-1} ± 0.17%; Renne et al., 2010); b) Selected whole-rock geochemical data vs. muscovite $^{40}Ar/^{39}Ar$ dates for each analyzed sample.

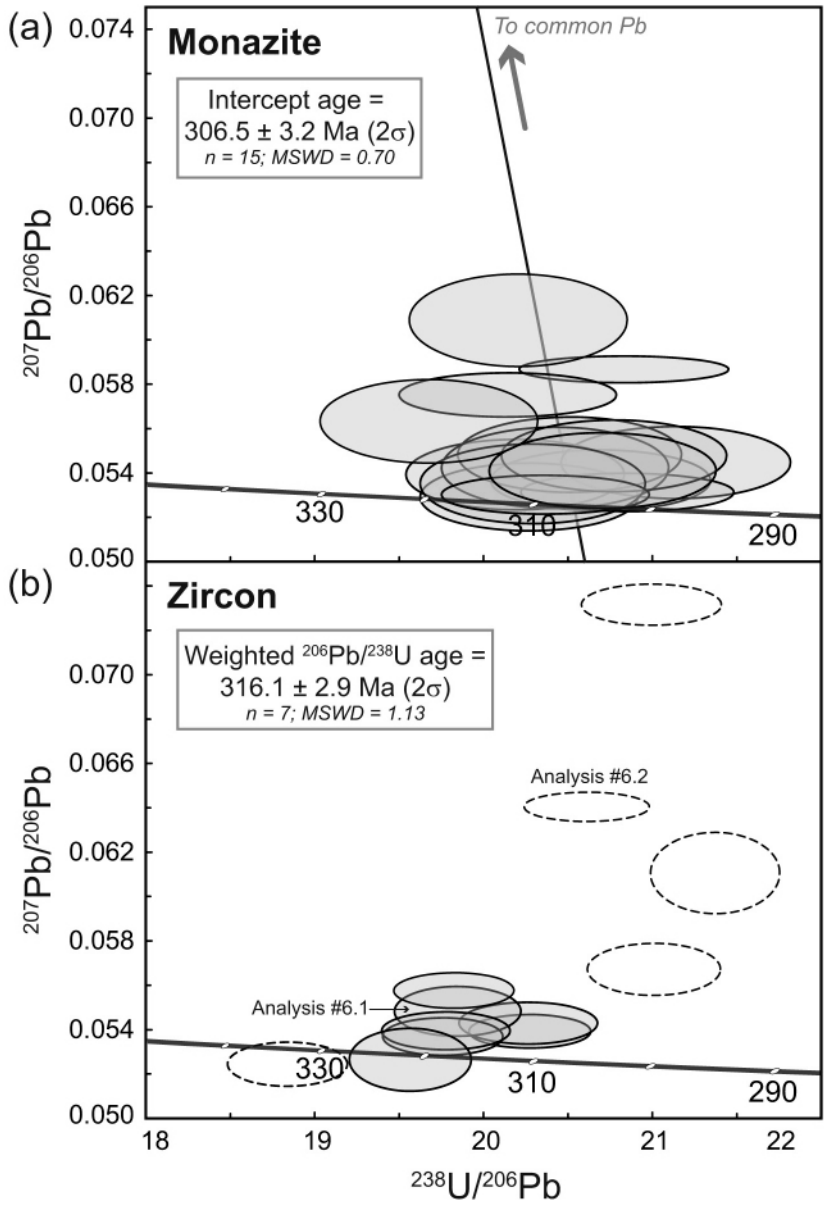


Figure 3: a) Tera-Wasserburg U-Pb diagram for monazite data from the sample QRT07; b) Tera-Wasserburg U-Pb diagram for zircon data from the sample QRT07. In these two diagrams, error ellipses are at 1σ. The intercept age has been calculated for all the monazite analyses and the $^{206}Pb/^{238}U$ weighted mean age for the seven zircon analyses filled in grey.

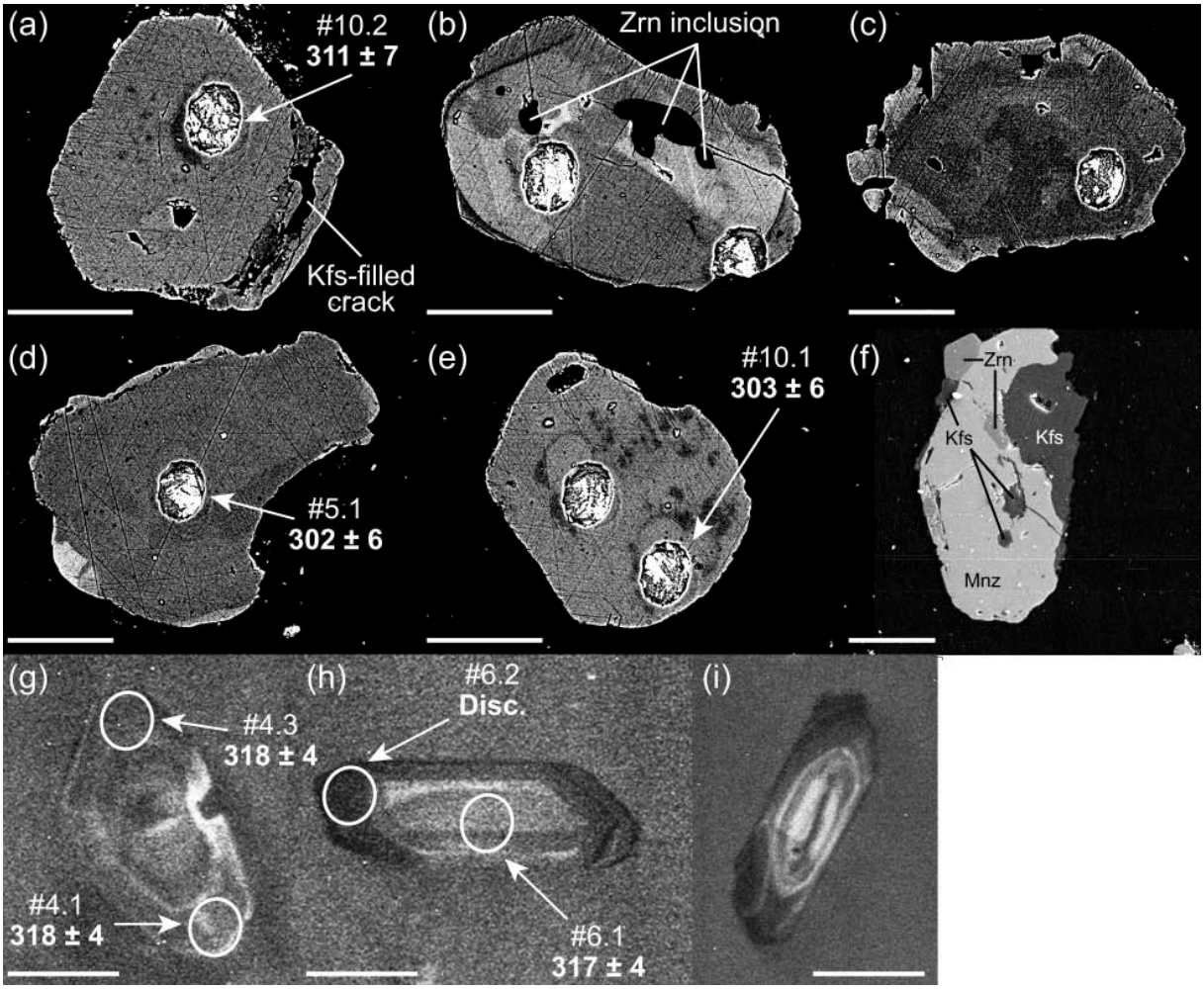


Figure 4: Selected images of monazite and zircon grains. a-e) Monazite grains (BSE images). Analysis numbers and corresponding $^{206}Pb/^{238}U$ dates are reported (1σ error). SHRIMP spots where no date is reported correspond to pits made during oxygen isotope analyses. f) SE image showing Zrn + Kfs intergrowths on a monazite grain. g-i) Zircon grains (CL images). Circles indicate the location of analyses. Analysis numbers and corresponding $^{206}Pb/^{238}U$ dates are reported (1σ error). Mineral abbreviations are after Whitney and Evans (2010). Scale bars represent 50 μm in all the pictures.

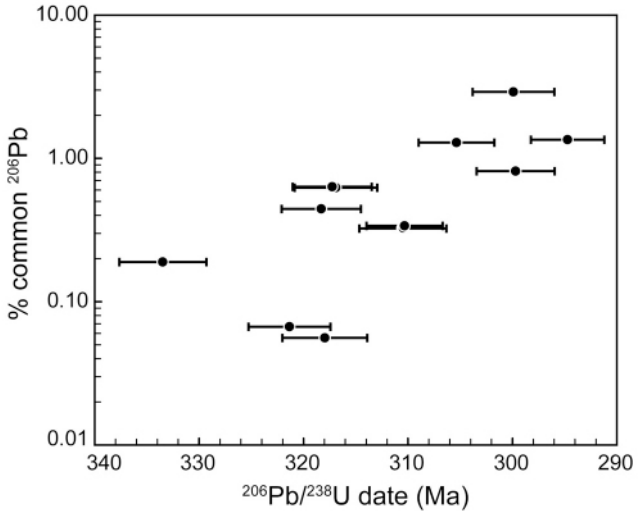


Figure 5: Percent of common ^{206}Pb against the zircon $^{206}Pb/^{238}U$ apparent dates.

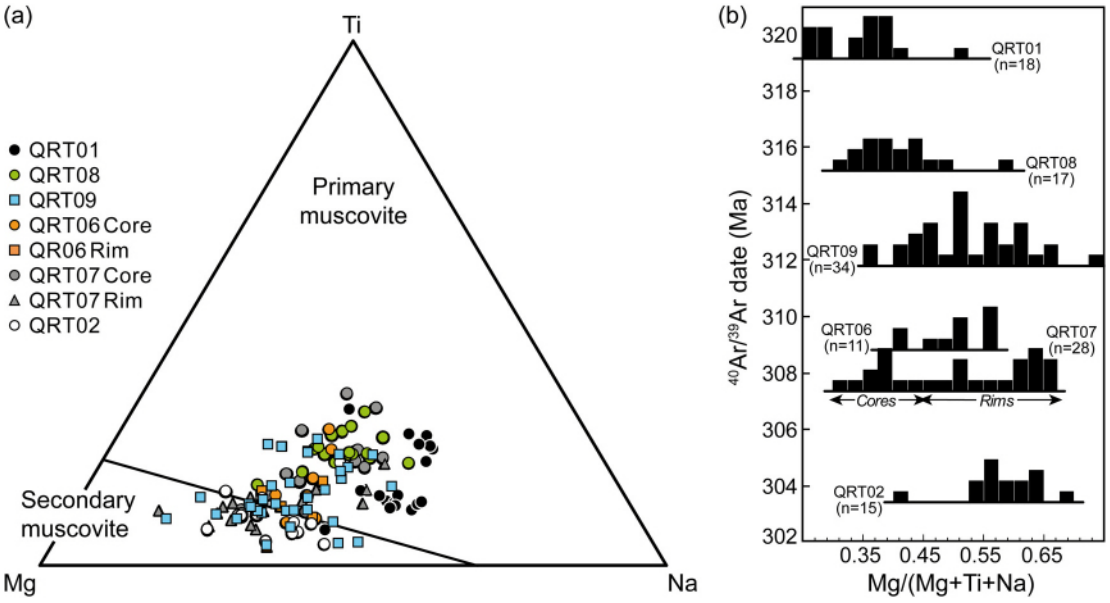


Figure 6: a) Muscovite chemical compositions plotted in the ternary Mg-Ti-Na diagram of Miller et al. (1981); b) $^{40}Ar/^{39}Ar$ dates vs. Mg/(Mg+Ti+Na) for each analyzed muscovite grain. The Mg/(Mg+Ti+Na) molar ratio illustrates the shift from primary to secondary muscovite fields in the ternary diagram.

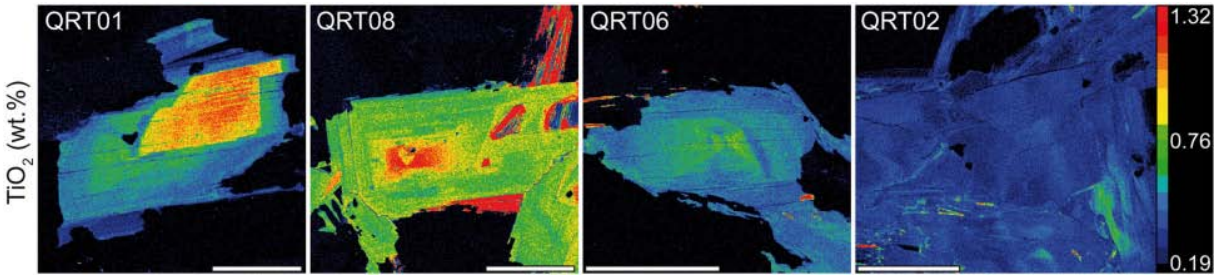


Figure 7: Chemical maps of TiO_2 distribution in muscovite grains from four samples. All images have the same color scale. Scale bars are 200 µm for samples QRT01 and QRT02 and 500 µm for samples QRT08 and QRT06.

Table 1: Muscovite ^{39}Ar-^{40}Ar analytical data.

Step	$^{40}Ar_{Atm}$ (%)	$^{39}Ar_K$ (%)	$^{37}Ar_{Ca}/^{39}Ar_K$	$^{40}Ar^*/^{39}Ar_K$	Age (Ma)[1]	1σ (Ma)
QRT01 Muscovite						
1	39.09	0.1	0.204	23.46	228.1	42.9
2	8.50	0.3	-	31.85	303.1	18.2
3	1.40	0.1	-	35.18	332.1	29.3
4	1.65	0.9	-	34.89	329.6	6.4
5	1.46	0.5	-	34.98	330.3	12.0
6	0.92	6.0	-	33.75	319.7	1.2
7	0.54	14.6	0.005	33.67	319.0	0.8
8	0.27	16.2	0.011	33.69	319.2	0.6
9	0.67	9.9	0.025	33.68	319.1	1.1
10	0.28	17.0	0.011	33.67	319.0	0.7
11	0.40	5.8	0.008	33.68	319.1	1.4
12	0.57	3.4	-	33.66	319.0	2.2
13	0.16	9.5	0.003	33.75	319.7	0.8
14	0.06	8.9	0.003	33.80	320.2	0.9
Fusion	0.52	6.6	0.002	33.63	318.7	0.9
QRT02 Muscovite						
1	28.84	0.6	0.050	28.05	269.4	7.2
2	3.61	2.2	0.047	32.65	309.9	2.0
3	3.63	1.2	-	32.43	308.1	3.7
4	1.29	17.1	0.020	31.87	303.2	0.5
5	0.74	2.5	0.026	31.96	303.9	2.1
6	1.19	20.5	0.017	31.84	302.9	0.5
7	0.40	14.3	0.011	31.95	303.9	0.5
8	0.51	9.2	0.016	31.87	303.2	0.9
9	0.40	9.8	0.019	31.95	303.9	0.6
10	0.19	16.6	0.022	31.92	303.6	0.7
Fusion	0.21	6.1	0.018	31.98	304.1	0.9
QRT06 Muscovite						
1	9.53	0.0	0.663	28.49	273.2	113.8
2	14.13	0.2	-	31.95	303.7	18.9
3	4.42	0.5	-	34.06	322.1	7.9
4	1.91	0.4	-	33.99	321.4	7.7
5	3.53	1.2	-	33.20	314.6	2.2
6	4.45	0.4	0.214	31.93	303.5	14.6
7	0.55	36.4	0.011	32.42	307.9	0.5
8	0.70	2.3	0.078	32.29	306.7	2.5
9	-	4.7	-	32.70	310.3	1.0
10	0.29	11.5	0.015	32.50	308.6	0.6
11	0.10	9.9	0.020	32.57	309.1	0.7
12	0.10	10.7	0.006	32.61	309.5	0.9
13	0.05	7.3	0.024	32.78	311.0	0.9
14	0.14	7.7	0.017	32.70	310.3	0.8
Fusion	-	6.8	0.016	32.91	312.1	1.0
QRT07 Muscovite						
1	20.41	1.1	-	32.35	307.0	4.0
2	6.48	0.8	-	33.79	319.6	6.0
3	13.06	1.0	0.030	32.73	310.4	5.2
4	1.96	28.8	0.007	32.42	307.7	0.5
5	0.42	3.0	0.005	32.28	306.5	1.4
6	0.58	7.3	0.003	32.45	308.0	0.9
7	0.31	8.0	0.003	32.38	307.3	0.7
8	0.61	18.8	0.011	32.33	306.9	0.6

9	0.35	17.8	0.010	32.37	307.3	0.6
10	0.52	6.6	0.020	32.43	307.7	1.0
Fusion	0.71	6.9	0.014	32.57	309.0	1.1
QRT08 Muscovite						
1	64.13	0.2	0.050	8.40	226.4	15.4
2	15.86	0.7	0.050	11.46	302.3	2.5
3	10.31	0.9	-	12.06	316.8	3.5
4	2.70	0.8	-	12.14	318.7	2.1
5	2.38	5.4	0.003	12.05	316.5	0.6
6	0.80	8.5	0.004	12.03	316.0	0.6
7	-	3.2	0.002	12.01	315.6	1.0
8	0.52	1.0	0.009	12.05	316.6	2.4
9	1.08	8.4	0.005	11.97	314.7	0.5
10	1.76	4.3	0.003	12.00	315.4	0.8
11	0.68	19.8	0.006	11.95	314.1	0.4
12	0.31	19.5	0.005	11.99	315.1	0.4
13	0.55	5.3	0.006	11.95	314.1	0.7
Fusion	0.15	21.9	0.005	12.02	315.8	0.5
QRT09 Muscovite						
1	59.12	0.0	0.034	7.00	190.8	68.1
2	39.01	0.1	0.063	7.59	206.1	45.6
3	20.20	0.2	0.053	11.73	309.2	17.7
4	29.06	0.1	-	9.77	261.1	50.3
5	11.37	0.6	-	11.85	312.1	3.4
6	5.16	0.7	0.002	11.93	314.0	3.3
7	2.58	0.5	-	12.00	315.6	5.5
8	2.16	0.7	-	11.98	315.2	2.7
9	4.79	1.3	0.001	12.00	315.6	1.6
10	0.41	6.2	0.004	11.88	312.6	0.8
11	1.00	3.3	0.005	11.80	310.9	1.1
12	1.03	2.7	0.010	11.84	311.8	1.1
13	0.42	7.7	0.005	11.85	312.1	0.6
14	0.14	8.7	0.004	11.84	311.8	0.5
15	0.25	12.5	0.005	11.84	311.9	0.5
16	0.05	12.0	0.006	11.84	311.7	0.5
17	0.13	20.1	0.006	11.83	311.5	0.4
18	0.23	15.3	0.007	11.84	311.8	0.6
19	0.08	4.1	0.012	11.92	313.8	0.7
Fusion	-	3.4	0.013	11.92	313.8	1.0

$^{40}Ar_{atm}$ = atmospheric ^{40}Ar; $^{40}Ar^*$ = radiogenic ^{40}Ar; Ca = produced by Ca-neutron interferences. K = produced by K-neutron interferences. [1]Age (Ma): the date is calculated using the decay constants recommended by Renne et al. (2010). The errors are at the 1σ level and include the error in the value of the J parameter (set to ± 0.2%). Correction factors for interfering isotopes produced by neutron irradiation in the McMaster reactor were $(^{39}Ar/^{37}Ar)_{Ca} = 7.06 \times 10^{-4}$, $(^{36}Ar/^{37}Ar)_{Ca} = 2.79 \times 10^{-4}$, $(^{40}Ar/^{39}Ar)_{K} = 2.97 \times 10^{-2}$.

Table 2: SHRIMP U-Pb results for the analyzed monazite and zircon grains from the sample QRT07.

Labels	$^{204}Pb/^{206}Pb$	$^{207}Pb/^{206}Pb$	1σ (%)	f_{206} (%)	$^{206}Pb/^{238}U$	1σ (%)	$^{207}Pb/^{235}U$	1σ (%)	$^{207}Pb/^{206}Pb$ Age (Ma)	1σ (Ma)	$^{206}Pb/^{238}U$ Age (Ma)	1σ (Ma)	$^{207}Pb/^{235}U$ Age (Ma)	1σ (Ma)	Disc. (%)
QRT07 Monazites															
2.1	0.0001	0.0537	1.7	0.22	0.0483	2.1	0.3575	2.7	357	6	304	6	310	8	15
3.1	0.0001	0.0529	1.9	0.20	0.0493	2.1	0.3599	2.8	325	6	310	7	312	9	4
4.1	0.0002	0.0545	2.0	0.46	0.0473	2.1	0.3551	2.9	390	8	298	6	309	9	24
4.2	0.0001	0.0539	1.9	0.16	0.0495	2.1	0.3682	2.9	368	7	312	7	318	9	15
5.1	0.0001	0.0531	1.1	0.14	0.0479	2.0	0.3512	2.3	334	4	302	6	306	7	10
6.1	0.0002	0.0548	2.0	0.40	0.0487	2.1	0.3684	3.0	404	8	307	7	318	9	24
7.1	0.0004	0.0587	0.7	0.79	0.0480	2.0	0.3881	2.1	554	4	302	6	333	7	45
8.1	0.0003	0.0575	1.1	0.64	0.0496	2.1	0.3936	2.4	511	6	312	7	337	8	39
9.1	0.0002	0.0542	2.2	0.28	0.0490	2.2	0.3659	3.1	380	9	308	7	317	10	19
10.1	0.0001	0.0548	1.9	0.19	0.0481	2.1	0.3634	2.9	403	8	303	6	315	9	25
10.2	0.0003	0.0609	2.3	0.48	0.0495	2.1	0.4154	3.1	635	14	311	7	353	11	51
11.1	0.0005	0.0535	2.2	0.92	0.0493	2.2	0.3636	3.1	350	8	310	7	315	10	12
12.1	0.0001	0.0530	1.1	0.12	0.0491	2.0	0.3589	2.3	330	4	309	6	311	7	6
16.1	0.0003	0.0541	2.1	0.60	0.0483	2.1	0.3602	3.0	375	8	304	7	312	9	19
17.1	0.0002	0.0563	2.2	0.32	0.0508	2.2	0.3947	3.1	465	10	320	7	338	10	31
QRT07 Zircons															
1.1	0.0007	0.0610	2.0	1.35	0.0468	1.2	0.3937	2.3	640	13	295	4	337	8	54
1.2	0.0004	0.0567	1.4	0.82	0.0476	1.2	0.3721	1.8	480	7	300	4	321	6	38
2.1	**0.0002**	**0.0543**	**1.2**	**0.32**	**0.0493**	**1.3**	**0.3693**	**1.8**	**383**	**4**	**311**	**4**	**319**	**6**	**19**
4.1	**-**	**0.0539**	**1.0**	**0.06**	**0.0506**	**1.3**	**0.3760**	**1.7**	**368**	**4**	**318**	**4**	**324**	**5**	**14**
4.2	**0.0002**	**0.0539**	**0.9**	**0.34**	**0.0493**	**1.2**	**0.3666**	**1.5**	**368**	**4**	**310**	**4**	**317**	**5**	**16**
4.3	**0.0002**	**0.0537**	**1.0**	**0.45**	**0.0506**	**1.2**	**0.3746**	**1.6**	**358**	**4**	**318**	**4**	**323**	**5**	**11**
6.1	**0.0003**	**0.0548**	**1.4**	**0.63**	**0.0504**	**1.2**	**0.3809**	**1.8**	**405**	**6**	**317**	**4**	**328**	**6**	**22**
6.2	0.0007	0.0640	0.7	1.29	0.0485	1.2	0.4283	1.4	743	5	305	4	362	5	59
7.1	0.0016	0.0731	0.8	2.91	0.0476	1.3	0.4803	1.5	1018	8	300	4	398	6	71
9.1	**-**	**0.0526**	**1.8**	**0.07**	**0.0511**	**1.2**	**0.3709**	**2.2**	**313**	**6**	**321**	**4**	**320**	**7**	**3**
11.1	**0.0003**	**0.0558**	**0.9**	**0.64**	**0.0504**	**1.2**	**0.3879**	**1.5**	**443**	**4**	**317**	**4**	**333**	**5**	**28**
13.1	0.0001	0.0524	1.2	0.19	0.0531	1.2	0.3838	1.8	304	4	334	4	330	6	10

Zircons analyses in bold are those used in the calculation of the $^{206}Pb/^{238}U$ weighted mean age.

Supporting Information for:

Simultaneous resetting of the muscovite K-Ar and monazite U-Pb geochronometers: a story of fluids

Romain Tartèse[1,2*], Gilles Ruffet[1,2], Marc Poujol[1,2], Philippe Boulvais[1,2] and Trevor R. Ireland[3]

[1]Université de Rennes 1, Géosciences Rennes, 35042 Rennes Cedex, France

[2]CNRS (CNRS/INSU) UMR 6118, Géosciences Rennes, 35042 Rennes Cedex, France

[3]Research School of Earth Sciences, Australian National University, Canberra, ACT 0200, Australia

Analytical procedures

Electron microprobe analyses

Muscovite chemistry (Supplementary Table 1) and chemical maps were acquired using a Cameca SX-100 electron microprobe at IFREMER, Plouzané, France operating in the wavelength-dispersive mode. Operating conditions were a 15 kV acceleration voltage, a beam current of 20 nA and a beam diameter of around 1 µm. Counting times were approximately 13-14 s per oxide for a standard spot analysis and it therefore took around 150 s for a complete analysis of the 11 oxides measured. For a complete description of the analytical procedure and the list of the standards used, see Pitra et al. (2008). WDS X-ray element maps have been realized in the same analytical conditions. The resolution for the different Ti maps is 1 µm/px for QRT01 and QRT02, 2 µm/px for QRT06 and 3 µm/px for QRT08 with a 100 ms dwell time per pixel.

Muscovite $^{40}Ar/^{39}Ar$ dating

Euhedral to subeuhedral single grains of muscovite, with variably deformed shapes resulting from syn-deformation crystallization, were handpicked from the 0.25–1.50 mm fractions. Two irradiations were performed at the McMaster reactor (Hamilton, Canada) and were monitored with Taylor Creek Rhyolite (TCR-2) sanidine (28.34 Ma, Renne et al. 1998). The first irradiation lasted 16.66 hr (total fluence of 1×10^{18} n.cm^{-2}) for samples QRT01, QRT02, QRT06 and QRT07 and the second irradiation lasted 43.33 hr (total fluence of 2.6×10^{18} n.cm^{-2}) for samples QRT08 and QRT09. Muscovite single grains were analyzed by step-heating with an $^{40}Ar/^{39}Ar$ laser probe, following the procedure described in Ruffet et al. (1991; 1995). Blanks were performed routinely each first or third step, and subtracted from subsequent sample gas fractions. A plateau age is obtained when apparent ages of at least three consecutive steps, representing a minimum of 70% of the ^{39}Ar released, agree within 2σ error bars with the integrated age of the plateau segment.

Zircon and monazite U-Th-Pb dating

Zircon and monazite were separated from the sample QRT07 with conventional heavy liquid and magnetic methods. Euhedral zircons are typically 100-200 µm long with elongation ratios of 2 to 3. Monazite grains are yellow, euhedral and stubby, with some grains displaying lobate edges. Individual grains were handpicked, mounted in epoxy,

hand-grounded, and polished on a lap wheel with 6 μm and 1 μm diamond suspension. Prior to analysis, all grains were photographed in transmitted and reflected light. Zircon grains were then imaged using cathodoluminescence (CL) imaging at the Electron Microscope Unit, Australian National University, Canberra, in order to reveal their internal structure. The CL investigation was performed with a HITACHI S2250-N scanning electron microscope working at 15 kV and 30 μA. Monazite grains were imaged using a JEOL JSM 6400 scanning electron microscope at the CMEBA laboratory (Rennes 1 University). Secondary electron (SE) images allow to display mineral intergrowths with monazite and back-scattered electron images reveal monazite internal structures.

Zircon and monazite were dated using the SHRIMP II and SHRIMP-RG, respectively, at the Research School of Earth Sciences (RSES, ANU). Analytical procedures for zircon dating followed the method described in Williams (1998). SHRIMP RG analyses of monazite (following the methodology of Williams et al., 1996) utilized energy filtering to remove lower-energy molecules from an isobaric interference at mass 204 (Ireland, 1995; Ireland et al., 1999). The primary oxygen ion beam excavated areas of *c.* 25-35 μm depth and *c.* 10-15 μm in diameter for zircon and monazite analyses respectively. The measured ratios were calibrated using reference zircon (TEM, 417 Ma, Black et al., 2004) and monazite (s44069, 425 Ma, Aleinikoff et al., 2006). As these two reference minerals are not homogeneous regarding U, Th and Pb, the contents have not been calculated for the studied samples. SHRIMP raw data were reduced using the Squid program of Ludwig (2001). U-Pb data uncorrected for common lead are presented in this study. Indeed, the exact quantification of the ^{204}Pb content is difficult to achieve (average 1σ uncertainty on the ^{204}Pb/^{206}Pb ratios is 23%), especially for Phanerozoic rocks (e.g. Price et al., 2006). Age calculations were done using the Isoplot/Ex software (Ludwig, 2008) and are given with errors at the 2σ level.

References

Aleinikoff, J.N., Schenck, W.S., Planck, M.O., Srogi, L., Fanning, C.M., Kamo, S.L. and Bosbyshell, H., 2006. Deciphering igneous and metamorphic events in high-grade rocks of the Wilmington Complex, Delaware: Morphology, cathodoluminescence and backscattered electron zoning, and SHRIMP U-Pb geochronology of zircon and monazite. *Geol. Soc. Am. Bull.*, **118**, 39-64.

Black, L.P., Kamo, S.L., Allen, C.M., Davis, D.W., Aleinikoff, J.N., Valley, J.W., Mundil, R., Campbell, I.H., Korsch, R.J., Williams, I.S. and Foudoulis, C., 2004. Improved $^{206}Pb/^{238}U$ microprobe geochronology by the monitoring of a trace-element-related matrix effect; SHRIMP, ID-TIMS, ELA-ICP-MS, and oxygen isotope documentation for a series of zircon standards. *Chem. Geol.*, **205**, 115-140.

Ireland, T.R., 1995. Ion microprobe mass spectrometry: Techniques and applications in cosmochemistry, geochemistry, and geochronology. In: Advances in Analytical Geochemistry (M. Hyman and M. Rowe, eds), **2**, 1-118.

Ireland, T.R., Wooden, J.L., Persing, H.M. and Ito, B., 1999. Geological applications and analytical development of the SHRIMP-RG. *Eos*, **80**, F1117.

Ludwig, K.R., 2001. Squid version 1.02: A user's manual. Berkeley Geochronology Center Special Publication, **2**, 21 pp.

Ludwig, K.R., 2008. Isoplot/Ex version 3.70: A geochronological toolkit for Microsoft Excel. Berkeley Geochronology Center Special Publication, **4**, 73 pp.

Pitra, P., Boulvais, P., Antonoff, V., Diot, H., 2008. Wagnerite in a cordierite-gedrite gneiss: witness of long-term fluid-rock interaction in the continental crust (Ile d'Yeu, Armorican Massif, France). Am. Mineral., **93**, 315-326.

Price, R.C., Ireland, T.R., Maas, R. and Arculus, R.J., 2006. SHRIMP ion probe zircon geochronology and Sr and Nd isotope geochemistry for southern Longwood Range and Bluff Peninsula intrusive rocks of Southland, New Zealand. *New Zeal. J.Geol. Geop.*, **49**, 291-303.

Ruffet, G., Féraud, G. and Amouric, M., 1991. Comparison of $^{40}Ar/^{39}Ar$ conventional and laser dating of biotites from the North Tregor batholiths. *Geochim. Cosmochim. Ac.*, **55**, 1675-1688.

Ruffet, G., Féraud, G., Ballèvre, M. and Kienast, J.R., 1995. Plateau ages and excess argon in phengites - An ^{40}Ar-^{39}Ar laser probe study of alpine micas (Sesia zone, Western Alps, northern Italy). *Chem. Geol.*, **121**, 327-343.

Renne P.R., Swisher, C.C., Deino, A.L., Karner, D.B., Owens, T.L. and DePaolo, D.J., 1998. Intercalibration of standards, absolute ages and uncertainties in $^{40}Ar/^{39}Ar$ dating. *Chem. Geol.*, **145**, 117-152.

Williams, I.S., 1998. U-Th-Pb Geochronology by Ion Microprobe. In: Applications of Microanalytical Techniques to Understanding Mineralizing Processes (M.A. McKibben,

W.C. Shanks III and W.I. Ridley, eds). Reviews in Economic Geology, Society of Economic Geologists, **7**, 1-35.

Williams, I.S., Buick, I.S. and Cartwright, I., 1996. An extended episode of early Mesoproterozoic metamorphic fluid flow in the Reynolds Range, central Australia. *J. Metam. Geol.*, **14**, 29-47.

138 Table 1: Average chemical composition of muscovite.

	QRT01 (n=15)	sd	QRT08 (n=17)	sd	QRT09 (n=34)	sd	QRT06 Core (n=7)	sd	QRT06 Rim (n=4)	sd	QRT07 Core (n=15)	sd	QRT07 Rim (n=13)	sd	QRT02 (n=15)	sd
SiO_2	46.17	0.62	45.89	0.73	45.40	0.50	44.69	0.28	44.94	0.34	46.46	0.42	46.19	0.21	46.17	0.62
TiO_2	0.26	0.13	0.77	0.27	0.46	0.21	0.50	0.24	0.39	0.11	0.65	0.32	0.35	0.14	0.26	0.13
Al_2O_3	34.17	1.03	35.42	0.59	35.41	0.78	34.36	0.34	34.63	0.46	34.48	0.49	34.19	0.67	34.17	1.03
FeO	2.84	1.24	1.39	0.29	1.92	0.40	1.86	0.20	1.88	0.19	2.23	0.58	2.49	0.56	2.84	1.24
MnO	0.13	0.06	0.00	-	0.01	0.03	0.01	0.04	0.01	0.05	0.10	0.04	0.12	0.05	0.13	0.06
MgO	0.82	0.11	0.75	0.13	0.85	0.14	0.79	0.09	0.80	0.04	0.78	0.11	0.82	0.13	0.82	0.11
Na_2O	0.35	0.06	0.67	0.14	0.42	0.10	0.43	0.02	0.40	0.07	0.46	0.13	0.38	0.13	0.35	0.06
K_2O	11.15	0.35	10.92	0.30	10.94	0.21	11.21	0.09	11.26	0.16	11.04	0.29	11.24	0.21	11.15	0.35
SUM	95.89		95.82		95.41		93.84		94.31		96.20		95.78		95.89	
Structural formula based on 11 oxygen atoms																
Si	3.09	0.02	3.05	0.02	3.04	0.02	3.05	0.01	3.05	0.02	3.09	0.02	3.09	0.01	3.09	0.02
Ti	0.01	0.01	0.05	0.01	0.02	0.01	0.03	0.01	0.02	0.01	0.03	0.02	0.02	0.01	0.01	0.01
Al	2.70	0.05	2.75	0.03	2.79	0.04	2.76	0.02	2.77	0.03	2.70	0.04	2.70	0.04	2.70	0.05
Fe	0.16	0.07	0.09	0.01	0.11	0.02	0.11	0.01	0.11	0.01	0.12	0.03	0.14	0.03	0.16	0.07
Mn	0.01	-	0.00	-	0.00	-	0.00	-	0.00	-	0.01	-	0.01	-	0.01	-
Mg	0.08	0.01	0.08	0.01	0.09	0.01	0.08	0.01	0.08	-	0.08	0.01	0.08	0.01	0.08	0.01
Na	0.05	0.01	0.08	0.01	0.05	0.01	0.06	-	0.05	0.01	0.06	0.02	0.05	0.02	0.05	0.01
K	0.95	0.02	0.94	0.02	0.93	0.02	0.98	0.01	0.98	0.02	0.94	0.03	0.96	0.02	0.95	0.02
SUM	7.05		7.04		7.03		7.06		7.06		7.03		7.05		7.05	

139 *Oxide contents in wt.% and cationic contents in apfu; sd = standard deviation (1σ).*